# Particle impact on metal substrates with application to foreign object damage to aircraft engines

## Xi Chen*, John W. Hutchinson

*Division of Engineering and Applied Sciences, Harvard University, Cambridge, MA 02138, USA*

**Abstract**

Foreign object damage (FOD) occurs when hard, millimeter-sized objects such as gravel or sand are ingested into aircraft jet engines. Particles impacting turbine blades at velocities up to about 300 m/s produce small indentation craters which can become sites for fatigue crack initiation, severely limiting the lifetime of the blade. A framework for analyzing FOD and its effect on fatigue cracking is established in this paper. Finite element analysis is used to determine the residual stresses and geometric stress concentration resulting from FOD. The roles of material rate sensitivity and inertia are delineated. The most important non-dimensional parameters governing impact indents are identified, significantly reducing the set of independent parameters. The second step in the analysis focuses on the potency of cracks emerging from critical locations at the indents. The results have been used to address the question: When and to what extent do the residual stresses and stress concentration caused by FOD reduce the critical crack size associated with threshold fatigue crack growth? For deep indents, it is found that elastic stress concentration is the dominant factor in reducing critical crack threshold when the applied cyclic load ratio, $R$, is large, otherwise the residual stresses are also important. Comparisons with a set of experiments conducted in parallel with the theory show that the numerical approach can account for various phenomena observed in practice. © 2002 Elsevier Science Ltd. All rights reserved.

*Keywords:* Fatigue; Foreign object damage; A. Impact; B. Critical crack size; C. Finite element

## 1. Introduction

During the course of their lives, the engines of aircraft, both military and civil, ingest foreign objects of various sorts. Ingestion of stones, sands, debris, rivet mandrels, bits of

---

* Corresponding author. Fax: +1-617-495-9837.
  *E-mail address:* chen@esag.harvard.edu (X. Chen).

tire, etc, is referred as "hard body" ingestion. The resulting damage is called foreign object damage or simply, FOD (Cowles, 1996; Larsen et al., 1996). FOD by hard particles mainly occurs during motion of the aircraft on the airfield, during takeoff and landing. Typically, the sizes of these hard particles are in the millimeter regime, with impact velocities determined primarily by the blade speed and in the range of 100–350 m/s, depending on the specific engine (Ritchie et al., 1999a). Most FOD occurs as damage to the leading edges of the front end, low-temperature turbine blades, typically made of Ti–6Al–4V alloy (Nicholas et al., 1980). FOD can cause significant amounts of damage to the blades and vanes in the compressor section of an engine. Smaller-sized foreign objects also strike the turbine blades in the high-temperature turbine section of gas turbine engines, causing severe damage to the thermal barrier coatings (Nicholls et al., 1997; Chen et al., 2002).

The typical load history experienced by an engine blade includes low-cycle fatigue (LCF) loading due to normal start–flight–landing cycles, and high-cycle fatigue (HCF) loading due to vibrations and resonant airflow dynamics, often superimposed on a high mean stress (Cowles, 1996; Mall et al., 2001). Under such cyclic loads, the micro-structural damage caused by FOD can lead to fatigue crack formation and propagation, thereby degrading component lifetime and causing unexpected HCF failures in critical engine components (Nicholas, 1999; Ritchie et al., 1999b; Peters et al., 2000). To investigate the influence of FOD on the HCF properties of Ti–6Al–4V alloy, experimental simulation has been conducted by Peters et al. (2000). In their experiments, hardened steel spheres (with diameter 3.2 mm) were used to normally impact a flat Ti–6Al–4V alloy specimen at 200–300 m/s. Scanning electron micrograph of impact damage site is presented in Fig. 1(a) for 300 m/s FOD. After impact, the specimens were cycled at a maximum nominal stress of 500 MPa (about half of the yield stress of Ti–6Al–4V) at a cyclic load ratio of $R = 0.1$. The authors found that FOD provides sites for the initiation of small radial fatigue cracks, which then propagate under the HCF spectra of large numbers of cycles ($> 10^9$). For the lower-speed impacts (200–250 m/s), crack initiation was observed to occur at the bottom of the indent at about 65,000 cycles, and the crack size was doubled after another 5000 cycles. For the 300 m/s high-speed impact, a prominent crater rim was produced and this turns out to be the site of the crack initiation after 35,000 cycles, which then grew to 6 times of its original size after another 10,000 cycles, as shown in Fig. 1(b). In both cases, the shape of the growing fatigue crack is almost semi-circular.

Of particular significance is the finding of Peters et al. (2000) that crack initiation in the vicinity of FOD occurs at cycle lifetimes that are orders of magnitude lower than found for un-impacted specimens. High-speed impacts were also observed to have caused micro-structural distortion in the form of shear bands emanating from the surface of the crater of 300 m/s FOD, although it was not evident that they had any effect on the fatigue life. Shear bands were not observed for lower-speed impacts.

Due to its influence on the high-cycle fatigue properties of key engine components, as described above, FOD is a prime cause for maintenance and repair in aircraft engines. The resulting costs of damage have been estimated at $4 billion annually for the civil aerospace industry, and the maintenance budgets for the UK and US Air Forces run into many millions of dollars each year, just attributable to FOD (Boyce et al.,
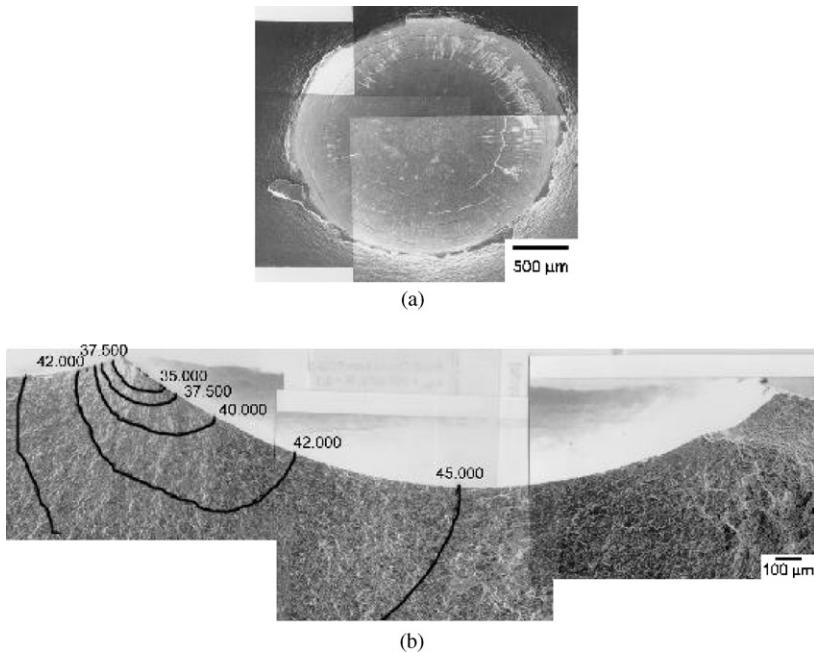
Fig. 1. Scanning electron micrograph showing (a) the impact site and (b) the growth of fatigue cracks initiated at 300 m/s FOD (Peters et al., 2000). The progressive position of the crack front is marked on the fracture surface as a function of number of load cycles (with maximum nominal stress of 500 MPa at a load ratio of 0.1). Courtesy J.O. Peters.

2001b). Despite the importance of this problem, current lifetime prediction and design methodologies for turbine engines still rely principally on empirical safety factors to account for FOD, rather than on an approach-based understanding of the salient mechanisms involved. One of the biggest challenges in the prevention of FOD-related failures lies in understanding the nature of the damage caused by the FOD impact. The extremely high number of cyclic loads typical of in-flight loading dictate that a defect-tolerant design approach be based on a crack propagation threshold, to ensure that the HCF-critical turbine components are operated below the fatigue crack propagation threshold $\Delta K_{TH}$. Only then, can one be confident that significant crack propagation will not occur within $10^9$ cycles (Boyce and Ritchie, 2001a).

Three elements of the mechanics of FOD need to be addressed:

(i) *Stress concentration by the FOD-induced impact sites*: FOD creates stress-raising indents that change the local stress pattern in the vicinity of the impact sites under applied load.

(ii) *Residual stresses induced by the FOD impact*: FOD induces a residual stress field due to the plastic deformation associated with the indent, which increases (or decreases) the stress acting on a small fatigue crack initiated at the site. As such, the residual stress can have profound influence on whether a putative fatigue crack grows

into a full-fledged fatigue crack, determining its location, initiation and propagation when superimposed with cyclic loading and stress concentration (Boyce et al., 2001b; Peters et al., 2002).

(iii) *FOD-induced micro-cracking and micro-structural distortion* (i.e. shear bands, local texturing): In blade alloy Ti–6Al–4V, micro-cracks are observed at the crater rim of the damage site when the impact velocity is larger than 300 m/s. The presence of such micro-cracks provides a potent site for fatigue cracks to nucleate under high-cycle fatigue loading (Peters et al., 2000, 2002).

As already mentioned, most FOD occurs as damage to the leading edges of turbine blades. However, in this study, to gain insight into the interaction between FOD and fatigue cracking, we have considered the less frequent form of FOD wherein the damage is assumed to occur away from the edge. The present paper generalizes and extends earlier work by Chen and Hutchinson (2001) that focused on fatigue cracking outside moderately shallow, statically induced indents for which stress concentration was not of dominant importance. The earlier work will be extended into the deep indentation regime, representative of high-velocity impacts, accounting for, and assessing the importance of, inertia and material strain-rate dependence in the impact analysis. The relative importance of geometric stress concentration and residual stress in altering the fatigue crack threshold will be examined as well. The present study has been coordinated with parallel experimental studies on FOD on flat surfaces of the blade material Ti–6Al–4V (Peters et al., 2000, 2002; Boyce et al., 2001b).

The next section sets the stage for the present paper by briefly reviewing the earlier study of Chen and Hutchinson (2001) on the influence of statically induced, moderately shallow FOD indents. Relevant material data on Ti–6Al–4V will also be introduced. The mechanics of the dynamic FOD impact problem is investigated in Section 3 with details presented for geometric stress concentration at the bottom and rim of the impact indent and for the residual stress distribution. Then, in Section 4, the effect of the FOD indent on putative fatigue cracks will be assessed with emphasis on whether, and to what extent, FOD decreases the critical threshold crack size. The paper ends with a discussion of other aspects of FOD and further potential applications of the approach.

## 2. Statically induced, moderately shallow indents and their influence on the critical size of threshold fatigue cracks

The earlier work of Chen and Hutchinson (2001) considered the quasi-static, axisymmetric normal impression of a hard spherical particle into a thick elastic–plastic substrate. As sketched in Fig. 2, a rigid sphere of diameter $D$ is pushed into a half-space by a static load $P$. The indentation load is then removed such that the contact diameter is $w$ and the indent depth is $\delta$, both measured after unloading. The material is taken to be elastic–ideally plastic with tensile yield stress $\sigma_Y$, Young's modulus $E$ and Poisson's ratio $v$. This representation is realistic for the Titanium alloy, Ti–6Al–4V, which has very low strain hardening (Ritchie et al., 1999a) with $E = 116$ GPa, $\sigma_Y = 930$ MPa and $v = 0.34$. The half-space is taken to be initially stress free and infinitely deep,
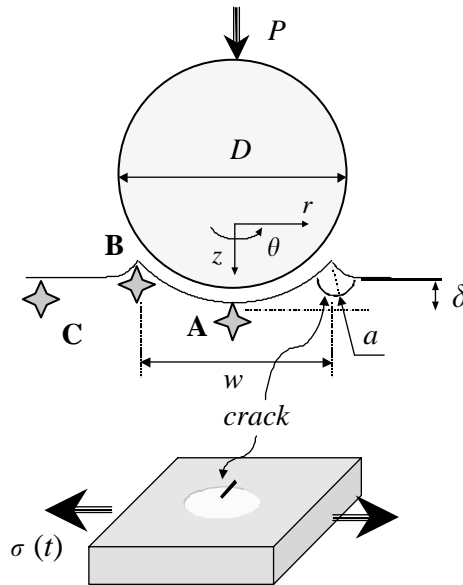
Fig. 2. A semi-circular surface crack with radius $a$ is embedded inside the residual stress field of the indent and subjected to cyclic stress $\sigma(t)$. The three most likely fatigue cracking sites are denoted by A, B, and C, respectively.

consistent with the assumption that the foreign object is small compared to the substrate thickness. A dimensionless load factor is denoted by

$$L \equiv \frac{P}{(\pi/4)D^2\sigma_Y}. \tag{1}$$

In the regime designated as moderately shallow indents by Chen and Hutchinson (2001) for which $0.006 < L < 0.4$, the load is related to the indent width, $w$, by $P \cong 2.3\sigma_Y w^2$ (see Fig. 2) and the depth, $\delta$, and width, $w$, of the indent are well approximated by

$$\frac{\delta}{D} \cong 0.07L, \quad \frac{w}{D} \cong 0.59\sqrt{L}. \tag{2}$$

These results are relatively insensitive to $\sigma_Y/E$ in the moderately shallow regime.

In the experimental studies, fatigue cracks nucleated at FOD sites developed and propagated on planes normal to the direction of the applied cyclic stress, as depicted in Fig. 2 (Peters et al., 2000; Boyce et al., 2001b). As a consequence, the residual stress component induced by the axisymmetric indent of most importance is the circumferential component, $\sigma_{\theta\theta}$. This component, scaled by $\sigma_Y$, was computed by Chen and Hutchinson (2001) using the commercial code ABAQUS (Hibbit and Karlsson & Sorensen Inc., 1999). The rigid contact surface option was used to simulate the rigid indenter, and the option for finite deformation and strain was employed. As already mentioned, the substrate material is taken to be elastic–perfectly plastic, with a Von Mises yield surface. Coulomb friction was invoked in the calculations, with the friction coefficient taken to be 0.1 to represent the case of nearly frictionless impact. The
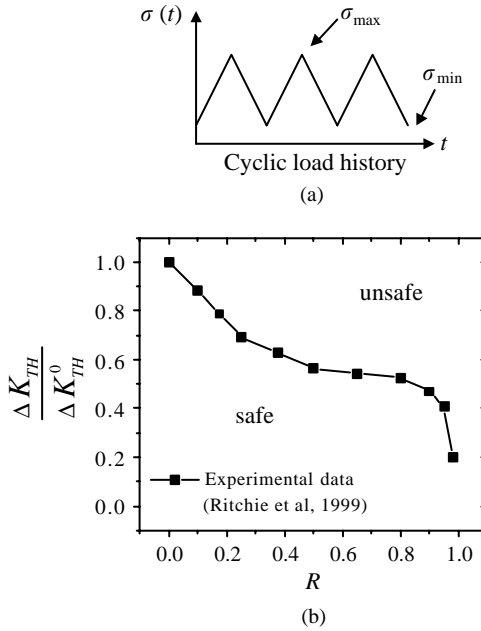
Fig. 3. (a) Illustration of the cyclic load history $\sigma(t)$; and (b) the material curve that characterizes the fatigue threshold property of Ti–6Al–4V.

yield strain, $\sigma_Y/E$, is found to be a minor factor on affecting $\sigma_{\theta\theta}/\sigma_Y$ since the load level corresponding to particle impact velocities of interest far exceeds the regime of elastic Hertzian indentation. The Poisson's ratio of the substrate and the friction are also shown to be relatively unimportant in the determination of the residual $\sigma_{\theta\theta}/\sigma_Y$ field surrounding a moderately shallow indent (see also Mesarovic and Fleck, 1999; Mall et al., 2001).

The computed residual stress distributions indicate three locations where residual stresses may enhance fatigue crack growth and lower the threshold of a surface crack. These regions where the residual hoop stresses are tensile, are designated by A, B, and C in Fig. 2; they are located at the center of crater floor, on the crater rim, and outside the rim, respectively. Now, imagine the half-space specimen is subjected to an applied cyclic loading history $\sigma(t)$ with a positive load ratio, simulating the high-cycle fatigue loading subsequent to the FOD. The following notation is used and illustrated in Fig. 3(a)

$$\begin{aligned}\sigma_{max} &\equiv \text{Max}[\sigma(t)] \\ \sigma_{min} &\equiv \text{Min}[\sigma(t)]\end{aligned}, \quad R_{applied} \equiv \sigma_{min}/\sigma_{max}. \tag{3}$$

Imagine a putative semi-circular crack of radius $a$ is located at one of the regions A, B or C. Symmetry dictates that the crack front is in Mode I. Identify the point on the front where the stress intensity factor, $K$, is the greatest. Let $\Delta K = K_{max} - K_{min}$ and $R = K_{min}/K_{max}$ where $K_{max}$ and $K_{min}$ are the maximum and minimum values experienced

under the cyclic loading $\sigma(t)$ in the presence of the residual stress. The stress intensity factors, $K_{max}$ and $K_{min}$, have been computed by Chen and Hutchinson (2001) using a full three-dimensional finite element analysis, accounting for the residual stress. The blade alloy Ti–6Al–4V has a threshold stress intensity factor, $\Delta K_{TH}$, below which cracks will not propagate under cyclic loading. This threshold has a strong dependence on the $R$ ratio for the crack tip cyclic load history, $R = K_{min}/K_{max}$. The fatigue crack data characterizing the curve of $\Delta K_{TH}$ vs. $R$ for the blade alloy Ti–6Al–4V (Ritchie et al., 1999a) is plotted in Fig. 3(b). Here, $\Delta K_{TH}^0 \equiv \Delta K_{TH}(R = 0)$ is a convenient reference value for normalization purposes ($K_{TH}^0 = 5$ MPa $\sqrt{m}$ for Ti–6Al–4V). A cubic functional form is used to fit the threshold data $\Delta K_{TH}/\Delta K_{TH}^0$ vs. $R$ in this plot:

$$\Delta K_{TH}/\Delta K_{TH}^0 = 1 + b_0 R + b_1 R^2 + b_2 R^3, \tag{4}$$

where for Ti–6Al–4V: $b_0 = -2.49$, $b_1 = 4.78$ and $b_2 = -3.12$. The functional form in Eq. (4) can be applied to other metals and alloys, although the coefficients will generally differ from material to material. As indicated in Fig. 3(b), a cyclic loading with ($\Delta K$, $R$) falling below the threshold line is safe in the sense that crack propagation will not occur.

Within the moderately shallow regime ($0.006 < L < 0.4$), the normalized maximum tensile residual hoop stress outside the rim of the indent, $\sigma_{\theta\theta}/\sigma_Y$, is found to be essentially independent of $L$. The indentation diameter, $w$, or, equivalently, the depth of the indent, $\delta$, is therefore the only scaling factor for moderately shallow indents. This simplifies the presentation of the residual stresses in this regime and makes it possible for approximate but accurate analytical expressions to be given for the stress intensity factor history, as described more fully by Chen and Hutchinson (2001). The residual stress acts throughout the imposed cyclic history, $\sigma(t)$. Thus, the residual stress raises the average level of $K$ but it does not contribute to $\Delta K$. In other words, residual tensile stress increases $R$, while $\Delta K$ is determined solely by $\sigma(t)$.

For a specimen with an indent of width $w$ that is subject to the cyclic history $\sigma(t)$, one can make use of the results for $\Delta K$ and $R$ just described to solve for the *critical crack size*, $a_c$ defined as the largest crack such that ($\Delta K, R$) falls on the threshold line in Fig. 3(b). Full details of the critical crack size determination for moderately shallow indents are given by Chen and Hutchinson (2001). As an example, consider putative semi-circular cracks located at point C in Fig. 2. There is no geometric stress concentration at this point. Plots of the dimensionless critical crack radius, $\bar{a}_c = a_c/(\Delta K_{TH}^0/\sigma_Y)^2$, as a function of $R_{applied} = \sigma_{min}/\sigma_{max}$ are shown Fig. 4 for a sequence of normalized indentation widths, $\bar{w} = w/(\Delta K_{TH}^0/\sigma_Y)^2$, in all cases for $\sigma_{max}/\sigma_Y = 1/4$. The upper curve labeled by $\bar{a}_c^0$ is the critical crack size in the absence of an indent ($\bar{w} = 0$). Indents smaller than about $\bar{w} = 2$ have essentially no effect on the size of the critical threshold fatigue crack, while indents larger than about $\bar{w} = 5$ reduce the normalized critical crack size to a limiting level designated by $\bar{a}_c^L$. This lower limit represents the case where the indent is sufficiently large (but still within the moderately shallow indentation regime) such that the local residual stress at C ($\sigma_{\theta\theta} = 0.24\sigma_Y$) fully surrounds the critical crack.

The normalized indentation size characterizing the two limiting critical crack sizes noted above was found to be essentially independent of $R_{applied}$. The transition range
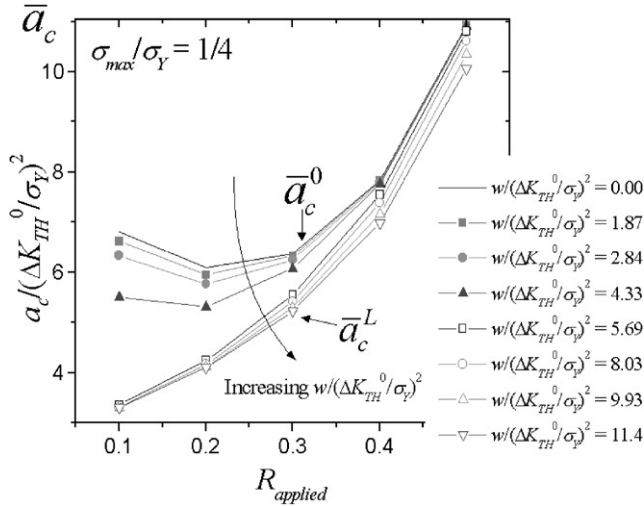
Fig. 4. The normalized critical crack threshold $\bar{a}_c$ is a function of $R_{applied}$, for a range of indentation sizes $\bar{w}$ with $\sigma_{max}/\sigma_y = 1/4$.
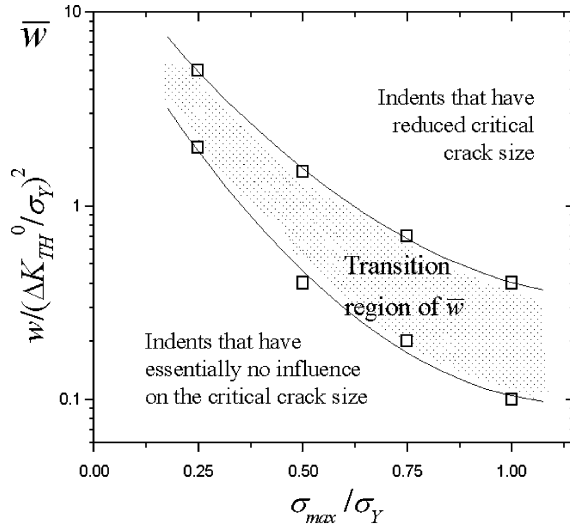


Fig. 5. Transition range of normalized indentation size as a function of $\sigma_{max}/\sigma_Y$ for moderately shallow indents. Indents below the transition have essentially no influence on the critical crack size, while indents above have the reduced critical crack size.

for the normalized indentation size as a function of $\sigma_{max}/\sigma_Y$ is shown in Fig. 5. For Ti–6Al–4V, which is a high-strength material, moderately shallow indents larger than 50 μm in diameter start to reduce critical crack size when $\sigma_{max}/\sigma_Y = 1/4$. By comparison, for mild steel the transition occurs at about $w = 11$ mm under the added constraint that the particle is sufficiently large such that shallow impact occurs.

The work by Chen and Hutchinson (2001) has focused on a special case of cracking outside moderately shallow indents (point C in Fig. 2). The studies has been repeated for the other two possible fatigue crack locations (A and B in Fig. 2), and behavior similar to that just described have been found (Chen, 2001). The characterization of the transition shown in Fig. 5 is robust for all three fatigue crack locations, and may be useful in establishing tolerable FOD levels as long as the indents are not deep. As stated earlier, this assertion is premised on the assumption that the FOD does not introduce new cracks larger than the critical size.

## 3. Dynamic aspects of FOD: deep indents

Discrepancies between the predictions based on quasi-static indentation analysis and the impact experiments conducted by Berkeley group (Boyce et al., 2001b) at the highest impact velocities motivated an extension of the analysis to account for both inertia and material strain-rate sensitivity. A rough estimate suggests strain rates in 300 m/s impacts should be well in excess of $10^4$ s$^{-1}$. Moreover, the deep crater caused by high-speed impact leads to significant stress-concentration effects, which, along with the residual stresses, contribute significantly to the reduction of critical crack size.

### 3.1. The mechanics of dynamic impact

The quasi-static results in Section 2 provide guidance to scaling the dynamic results. By Eqs. (1) and (2), it follows that the work of indentation, $W = \int P \, d\delta$, normalized as, $W/(\sigma_Y D^3)$, is a function of $\delta/D$, that is almost independent of the elasticity of the substrate. In dimensionless terms, this means that $W/(\sigma_Y D^3)$ is independent of $\varepsilon_Y = \sigma_Y/E$. The kinetic energy of the incoming particle is KE $= \frac{\pi}{12} D^3 \rho_p v_0^2$ with $\rho_p$ as the particle density and $v_0$ the impact speed. With $\sigma_Y D^3$ as the normalization factor, we define a dimensionless impact energy

$$\Omega = \text{KE}/(\sigma_Y D^3) = \frac{\pi}{12}(\rho_p/\sigma_Y)v_0^2. \tag{5}$$

It will be seen that $\Omega$ is the dominant dimensionless parameter in the dynamic problem. Moreover, it will be seen that the dimensionless time variable, $t\sqrt{\sigma_Y/\rho_p}/D$, correctly scales the temporal aspects of the phenomenon.

For a substrate material with a given strain-rate dependence, the general dimensionless form of the stress history is

$$\frac{\sigma_{ij}(\mathbf{x},t)}{\sigma_Y} = F_{ij}\left[\frac{\mathbf{x}}{D}, \frac{t\sqrt{\sigma_Y/\rho_p}}{D}, \Omega, \varepsilon_Y, \frac{\rho_p}{\rho}\right]. \tag{6}$$

The time-dependent history of indentation crater, which includes the indent depth $\delta(t)/D$, width $w(t)/D$ and pile-up $\delta^P(t)/D$, as well as the normalized foreign object speed $v(t)/v_0$, are all functions of the same variable set, $t\sqrt{\sigma_Y/\rho_p}/D$, $\Omega$, $\varepsilon_Y$, and $\rho_p/\rho$. Implicit is also a weak dependence on the friction coefficient and Poisson's ratio.

A significant further reduction of the variable set is revealed by the numerical results reported later in this section. Some reduction can be anticipated by noting that

numerical results for quasi-static indentation (Chen and Hutchinson, 2001) reveal that the normalized depth of a static indent, $\delta/D$, is a function primarily only of the normalized plastic work of indentation, $W/(\sigma_Y D^3)$. It is nearly independent of the elasticity of the substrate, measured by $\varepsilon_Y = \sigma_Y/E$. The results for dynamic impact presented later reveal, in addition, that $\rho_p/\rho$ has almost no effect on the results of interest when the dimensionless variable set noted above is used. Therefore, the primary dependence of the stresses in the substrate is found to be

$$\frac{\sigma_{ij}(\mathbf{x},t)}{\sigma_Y} = F_{ij}\left[\frac{\mathbf{x}}{D}, \frac{t\sqrt{\sigma_Y/\rho_p}}{D}, \Omega\right] \tag{7}$$

such that the residual stresses have the functional form:

$$\frac{\sigma_{ij}^R(\mathbf{x})}{\sigma_Y} = F_{ij}^R\left[\frac{\mathbf{x}}{D}, \Omega\right]. \tag{8}$$

Moreover, the residual parameters characterizing the FOD geometry, $\delta/D$, $w/D$, and $\delta^P/D$, depend primarily on $\Omega$: a remarkable collapse of a relatively large parameter set to a dependence on only one dimensionless variable.

The ricochet velocity, $v_b$, depends as well on the elasticity of the substrate, and for this purpose introduce $v_s \equiv \sqrt{E/\rho}$. The normalized ricochet velocity, $v_b/v_0$, depends on $\varepsilon_Y$ and $\rho_p/\rho$, in addition to $v_0/v_s$.

### 3.2. The finite element method

Dynamic finite element analyses are performed using ABAQUS/Explicit (Hibbit and Karlsson & Sorensen Inc., 1999) based on the explicit time integration method. This method is able to perform larger dynamic simulations than the implicit integration method and does not require iteration. The term *explicit* refers to the fact that the state at the end of the increment is based solely on the displacements, velocities, and accelerations at the beginning of the increment. The time increments in the explicit analysis are very small—a small fraction of the time for an elastic wave to traverse the smallest element and on the order of $10^{-10}$ s in the present case in dimensional terms. Strain-rate hardening is invoked in the simulation and takes the functional form of Eq. (9) introduced below. Local heating and its effect on the flow stress has been neglected based on estimates of adiabatic temperature changes obtained from computed plastic strains (Chen, 2001). The Coulomb friction coefficient is taken to be 0.1 as in the static indentation analysis. The substrate is taken to be semi-infinite and the axisymmetric mesh contains 25,600 4-node bilinear elements (with reduced integration). The rigid spherical projectile makes contact with the specimen with a specified initial speed, deforms the substrate as it comes to rest, and then bounces back after the impact. The histories of stress and strain fields are recorded during the numerical simulation along with the ricochet velocity and the final deformed geometry and residual stresses.

For most metals and alloys, the yield stress increases with increasing strain rate. The effect is relatively weak when strain rate is small, but some materials display a fairly dramatic increase in flow stress at strain rates above $10^3$–$10^4$ s$^{-1}$ (Clifton, 1983). The maximum strain rate generated from a 300 m/s FOD was found to be above this

range, and thus it is reasonable to expect rate sensitivity may be an important factor. For materials with negligible strain hardening, the rate dependence can be analytically expressed in a power-law form:

$$\dot{\varepsilon} = \dot{\varepsilon}_r \left( \frac{\sigma_Y(\dot{\varepsilon})}{\sigma_Y} - 1 \right)^n. \tag{9}$$

Here, $\dot{\varepsilon}$ is the strain rate, $\sigma_Y(\dot{\varepsilon})$ is the strain-rate sensitive yield stress, and $\sigma_Y \equiv \sigma_Y(0)$ the yield stress at $\dot{\varepsilon} \sim 0$, and $\dot{\varepsilon}_r$ is a constant with units $s^{-1}$. For Ti–6Al–4V we have taken $\dot{\varepsilon}_r = 2 \times 10^4$ 1/s and $n = 3$. This relationship (shown in the inset of Fig. 6) is largely consistent with the experimental data of Meyer (1984) in tension, showing a substantial increase in the yield stress at strain rates in excess of $10^3$ $s^{-1}$. This choice overestimates somewhat the rate-effect for Ti–6Al–4V shown in the compression data, Follansbee and Gray (1989). The same rate sensitivity has been consistently used to simulate parallel Berkeley experiments and agrees well with experimental measurements (see below and also Boyce et al., 2001b; Peters et al., 2002).

### 3.3. Numerical results

The time evolution of $\delta(t)/D$ during impact is displayed in Fig. 6(a) for the rate-dependent material for different combinations of $\varepsilon_Y$ and $\rho_p/\rho$, all with normalized kinetic energy $\Omega = 0.2$. The success of the time normalization, $t\sqrt{\sigma_Y/\rho_p}/D$, in capturing the relevant time scale of the phenomena is obvious. Except in the vicinity of the point of peak penetration (where the spring back is elastic), the history is essentially independent of $\varepsilon_Y$ and $\rho_p/\rho$. There is some dependency on $\varepsilon_Y$ and $\rho_p/\rho$ prior to peak penetration when these parameters are both small. Over most of the relevant range of the parameter set, however, the residual penetration depends almost entirely on $\Omega$. The ricochet velocity of the particle, $v_b$, is established during the segment of the history near the peak penetration as can be seen in the companion for the plots for the particle velocity in Fig. 6(b). The particle velocity is zero (at maximum penetration) at $t\sqrt{\sigma_Y/\rho_p}/D \cong 0.5$ and then becomes negative for all cases. The particle separates from the substrate at roughly $t\sqrt{\sigma_Y/\rho_p}/D \cong 0.6$, but with some dependence on $\varepsilon_Y$ and $\rho_p/\rho$. The elasticity of the substrate has a significant influence on the ricochet velocity causing more than a tripling of velocity for an eightfold decrease in Young's modulus, i.e. $\varepsilon_Y$ increasing from 0.001 to 0.008.

Residual depth of impact as a function of the kinetic energy of the incoming spherical particle is presented in Fig. 7 for a wide range of the dimensionless parameters. The inclusion of the large number of results has been done deliberately to reveal the dominant role of the dimensionless parameter $\Omega$. In addition, for reference, the quasi-static indentation result is included as the lower dash curve with the ordinate plotted as the normalized work of indentation, $W/(\sigma_Y D^3)$, rather than $\Omega$. This quasi-static result was computed with $\varepsilon_Y = 0.001$, but it is essentially independent of $\varepsilon_Y$ as previously discussed. Dynamic results computed without material rate dependence (as an elastic perfectly plastic material with $\sigma_Y(\dot{\varepsilon}) = \sigma_Y(0) \equiv \sigma_Y$ and $n = 0$ in Eq. (9)) fall between
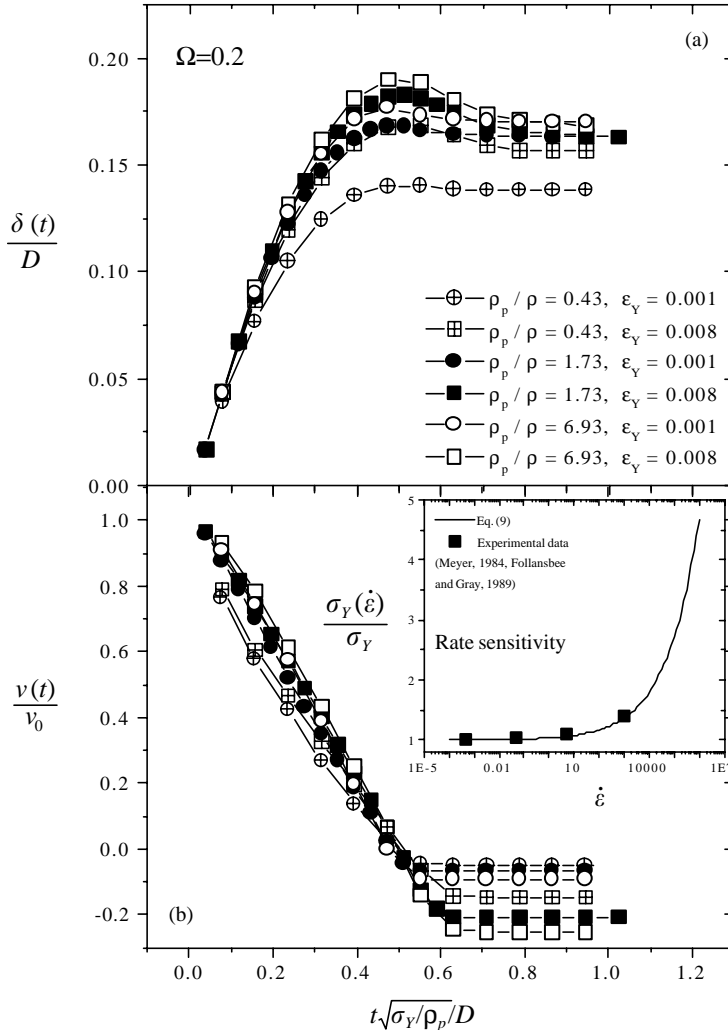
Fig. 6. (a) Normalized indent depth history $\delta(t)/D$ is essentially independent of $\varepsilon^{Y}_{tbc}$ and $\rho_p/\rho$ except at very high strain rates and except at the peak penetration just at the beginning of rebound. (b) The time history of the particle velocity $v(t)/v_0$ is varying with $\varepsilon^{Y}_{tbc}$ and $\rho_p/\rho$.

the quasi-static results and those that account for both inertia and material rate effects. [1] As expected, rate-dependent hardening as characterized by Eq. (9) reduces the depth of impact. At the highest impact velocities, the reduction is as much as 20% below the

---

[1] The one exception is for quite deep indents at low values of $\varepsilon_Y$ (the case for rate-independent behavior with $\rho_p/\rho = 0.43$ and $\varepsilon_Y = 0.001$ in Fig. 7) where the indents are even deeper than quasi-static indents. A new mechanism comes into play in this case associated with a cavitation instability during penetration caused by very high transient triaxial compressive stresses (Huang et al., 1991).
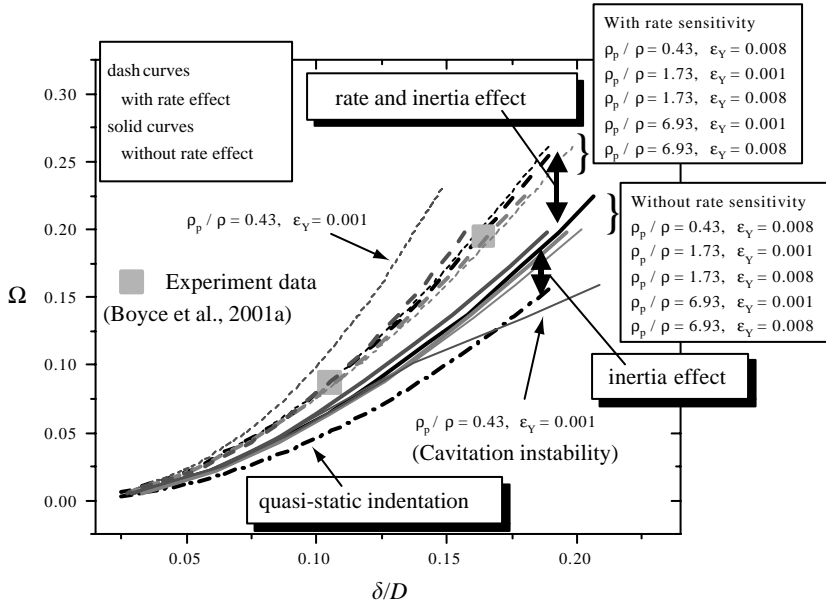
Fig. 7. The residual indent depth $\delta/D$ is a function primarily of $\sqrt{\Omega}$, except in cases where cavitation instabilities occur or where both $\rho_p/\rho$ and $\varepsilon_Y$ are small giving rise to extremely high strain rates. The rate and inertia effects are elaborated.

dynamic, rate-independent results and more than 40% below estimates based on the quasi-static results. The rate-dependent results are nearly independent of $\varepsilon_Y$ and $\rho_p/\rho$ over the entire range plotted, except for the case $\rho_p/\rho = 0.43$ and $\varepsilon_Y = 0.001$ which gives rise to exceptionally high strain rates in the substrate. Included in Fig. 7 are two experimental data points from Boyce et al. (2001b) for impact of steel spherical balls of 3.2 mm diameter at 200 and 300 m/s, affirming the effectiveness of the strain-rate sensitivity we have used for the Ti–6Al–4V.

In summary, Fig. 7 reveals that the residual indent depth primarily depends on the normalized incoming kinetic energy through $\Omega$, except for combinations of $\varepsilon_Y$ and $\rho_p/\rho$ when both quantities are small. When $\varepsilon_Y$ and $\rho_p/\rho$ are small, plastic deformation is either governed by extremely high strain rates (with smaller impact depths), or by cavitation instabilities in the absence of a material strain-rate effect (which cause larger impact depths). Nevertheless, for materials with the rate sensitivity representative of Ti–6Al–4V, to a good approximation the residual penetration is only a function of $\Omega$:

$$\bar{\delta} = \delta/D \approx 0.33\sqrt{\Omega}(1 + 0.24\sqrt{\Omega}). \tag{10}$$

The maximum plastic pile-up, $\delta^P$, is approximated by

$$\bar{\delta}^P = \delta^P/D = 0.27\sqrt{\Omega}(0.1 + 0.70\sqrt{\Omega}). \tag{11}$$

The normalized residual indent width, $w/D$, can be expressed in terms of the residual penetration and pile-up from simple geometric analysis:

$$w/D = 2\sqrt{\bar{\delta} + \bar{\delta}^P - (\bar{\delta} + \bar{\delta}^P)^2} \quad \text{when } \delta + \delta^P < D/2 \tag{12}$$

with $w \approx D$ when $\delta + \delta^P \geqslant D/2$. As already emphasized, Eqs. (10)–(12) are not valid in cases where both $\varepsilon_Y$ and $\rho_p/\rho$ are in the lower end of their typical ranges.

Fig. 7 might also be used to interpret dynamic effects in the following way. For a given material, the curve for the normalized quasi-static work of indentation, $W/(\sigma_Y D^3)$, can be determined from a single indentation test. With this experimental information in hand, Fig. 7 can be used to estimate the relation of particle velocity to indentation depth.

For the velocity of rebound, a function that fits over the range of parameters considered here is

$$v_b/v_0 \approx -95\varepsilon_Y(1 - 2.3\sqrt{v_0/v_s} - 24\varepsilon_Y). \tag{13}$$

Unlike Eqs. (10)–(12), this formula is only valid for a density ratio of $\rho_p/\rho = 1.73$, which is representative when a steel particle hits the titanium substrate. In Eqs. (10)–(13), the fitting functions are chosen such that they are consistent with the following general requirements: $\delta$, $\delta^P$, $w \to 0$ when $\Omega \to 0$, and $v_b/v_0 \to 0$ when $\varepsilon_Y \to 0$.

## 3.4. The elastic stress concentration factor for the indent

For deep indents, it is more convenient to consider the dimensional quantities functions of the indentation depth $\delta$ rather than the indentation width. The elastic stress concentration is tied to the surface geometry after impact. The elastic stress concentration factor ($k_t \equiv \sigma_{\theta\theta}/\sigma$, where $\sigma$ is the remote stress) as a function of position along the surface of the indent has been determined from three-dimensional finite element analysis. The three-dimensional mesh for the problem is developed by revolving the deformed axisymmetric mesh associated with the impact. Critical locations are at the crater floor and rim (A and B in Fig. 2). Stress concentration factors at these two locations are presented in Fig. 8 and compared with some early data from three-dimensional photoelastic experiments (Nisida and Kim, 1962). The comparison shows that the finite element result agrees well with experimental data at point B, whereas at point A the elastic stress concentration factor predicted from finite element analysis is about 7% larger than that of the experimental points. We believe the mesh refinement employed in the present numerical calculation is adequate to provide estimates of the stress concentration factor to within several percent.

## 3.5. Residual stresses

A residual hoop stress contour plot, $\sigma_{\theta\theta}/\sigma_Y$, is given in Fig. 9 for a normalized kinetic energy of $\Omega = \frac{\pi}{12}(\rho_p/\sigma_Y)v_0^2 = 0.2$, corresponding to the Berkeley experiments wherein a steel ball impacts Ti–6Al–4V at $v_0 = 300$ m/s (Peters et al., 2000, 2002; Boyce et al., 2001b). These results have been computed accounting for the material
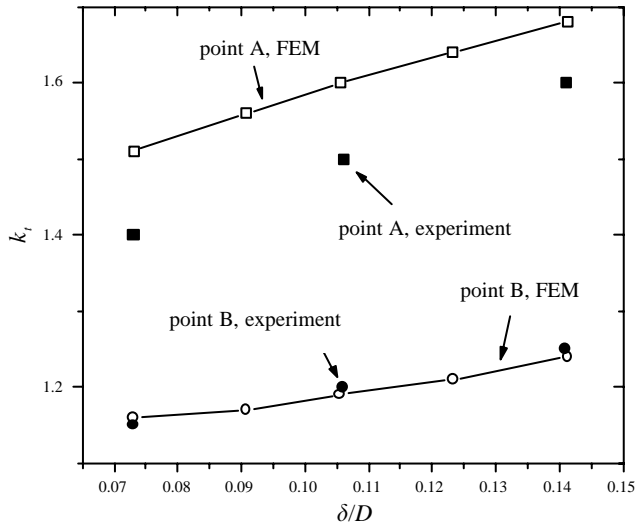
Fig. 8. The comparison between finite element analysis and experiment results (Nisida and Kim, 1962) on the elastic stress concentration factor $k_t$ as a function of $\delta/D$.
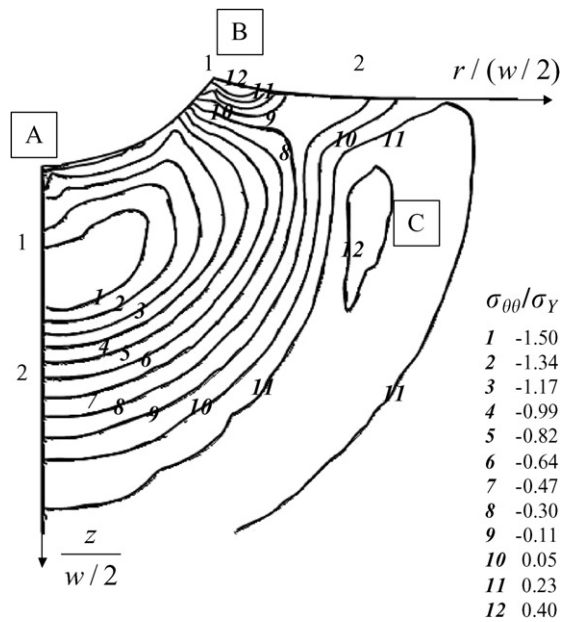


Fig. 9. Contour plot of the residual hoop stress field (normalized by $\sigma_Y$) in the vicinity of crater predicted from dynamic FEM. The normalized impact energy is $\Omega = 0.2$.
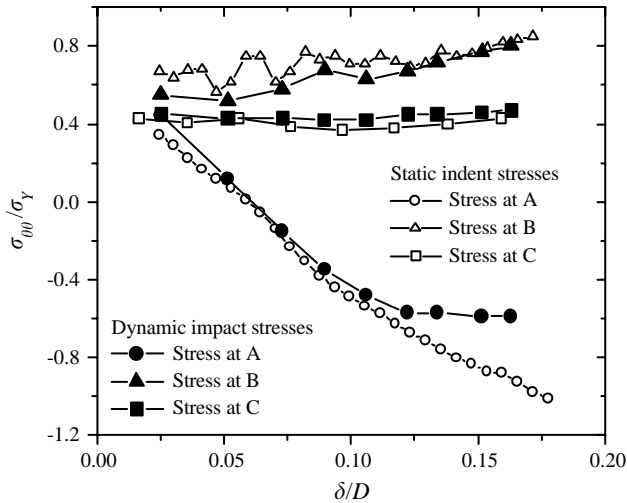
Fig. 10. Comparison between static and dynamic residual hoop stresses at critical locations A, B and C (cf. Fig. 9). The residual stresses primarily depend on $\delta/D$.

rate dependence and inertia. Of particular importance are two primary zones of tension, which will increase the local mean stress during subsequent fatigue loading. These regions of residual tension are: a small but intense region at the surface immediately outside the crater rim, denoted by B, and a broad subsurface region approximately one crater radius away from the crater, at C. The maximum residual tensile stress at both locations vary between $0.4\sigma_Y$ and $0.8\sigma_Y$, in general agreement with experiment measurements (Boyce et al., 2001b; Peters et al., 2002). Specifically, the subsurface stress at C was found to be within 10% of the prediction, while the measured stress at the rim showed more discrepancy probably due to the steep variation in the stress at that location and the small specimen size used in experiments. The most substantial compressive stresses, counterbalancing the residual tensile stresses, are formed beneath the crater. The maximum residual compressive component $\sigma_{\theta\theta}$ is about $-1.5\sigma_Y$ and is located one crater radius below the surface.

By Eq. (8), the residual stress field caused by a dynamic impact primarily depends on $\Omega$ (or, equivalently, by Eq. (10), on $\delta/D$). In principle the dimensionless parameters characterizing the material rate sensitivity, $n$ and $v_0/(D\dot{\varepsilon}_r)$, might also be expected to influence the residual stresses. In fact, however, the numerical studies reveal that, for the most part, rate dependence has relatively little influence on the residual stresses when they are expressed as a function of $\delta/D$. This can be seen in Fig. 10 where the residual stresses at the critical locations A–C are plotted as a function of $\delta/D$ for both quasi-static indentation and fully dynamic, rate-dependent impact. The comparison shows that the stresses caused by static and dynamic indents are quite close, except at the crater floor of deep impacts. The important conclusion to be drawn from Fig. 10 is that, the tensile stresses at locations B and C do not depend strongly on dynamic aspects of the impact when the depth of penetration, $\delta/D$, is used to determine the

residual stress. (Of course, the relation of $\delta/D$ to $\Omega$ in Fig. 7 does depend on dynamic aspects.)

## 4. Effect of FOD on fatigue cracking

The crater floor (A in Fig. 9) is characterized by a high elastic stress concentration factor (cf. Fig. 8), but compressive residual stress. The rim (B) has a smaller elastic stress concentration factor, but a residual tensile stress lying between $0.5\sigma_Y$ and $0.8\sigma_Y$ (cf. Fig. 10). The subsurface location C has essentially no elastic stress concentration but it has a residual tensile stress of about $0.4\sigma_Y$. Fatigue cracks have been observed to nucleate at all three locations (Peters et al., 2002). At high incident velocity (around 300 m/s in Berkeley experiments), the rim appears particularly susceptible to fatigue crack nucleation due to a combination of the stress concentration, residual tension and the formation of microcracks produced by the impact at the crater ridge. Fatigue crack growth is promoted at the rim from these microcrack sites, particularly when $\sigma_{max}/\sigma_Y$ is high ($\sigma_{max} \approx \frac{1}{2}\sigma_Y$) (Peters et al., 2002). In the section that follows, we analyze the effect of deep impact FOD on the critical crack size for cracks at the crater rim (point B).

### 4.1. Critical crack size for cracks nucleated at the rim

For a putative semi-circular crack of radius $a$ centered at the impact rim at the crater rim, there are two contributions to its mode I stress intensity factor: (i) due to residual stress, $K_{res}$, and (ii) due to cyclic loading (3), $\Delta K$.

(i) The analysis for $K_{res}$ makes use of a detailed three-dimensional finite element analysis to compute the maximum stress intensity factor along the perimeter of the putative crack produced by the full residual tensile stress field. The results are computed as a function of $a$ for each value of $\delta/D$ or, equivalently, each value of $w/D$. As already remarked, at the rim, the residual stress field depends primarily on $\delta/D$, with little dependence on dynamic effects. For the fatigue analysis it is useful to normalize $K_{res}$ by $\Delta K_{TH}^0$ and to employ the normalizations: $\bar{a}=a/(\Delta K_{TH}^0/\sigma_Y)^2$, $\bar{w}=w/(\Delta K_{TH}^0/\sigma_Y)^2$ and $\bar{D}=D/(\Delta K_{TH}^0/\sigma_Y)^2$. A functional fit of the finite element results over the full range of interest takes the following form (Chen, 2001):

$$K_{res}/\Delta K_{TH}^0 = \sqrt{\bar{a}}(d_0 + d_1\bar{a}/\bar{w})/\sqrt{\bar{w}/\bar{D}}, \tag{14}$$

where $d_0 = 0.2$ and $d_1 = -2.1$. Note that any choice of $\Delta K_{TH}^0$ can be used in this representation since it appears linearly in the denominator on both sides of the equation.

(ii) The stress intensity contribution due to the superimposed cyclic loading, $\Delta K$, is taken as $\Delta K = c_r\sigma(t)\sqrt{4a/\pi}$, where $\sigma(t)$ is the applied cyclic stress (3). The factor $c_r$ reflects both the stress concentration (Fig. 8) and the sharpened geometry of the rim (Fig. 2). It is obtained from a three-dimensional finite element calculation for a
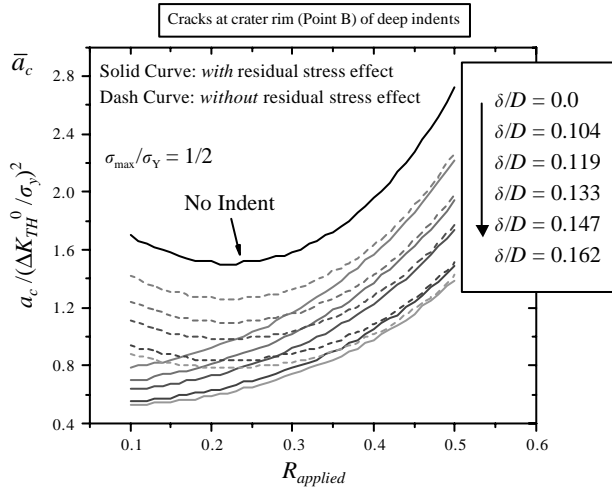
Fig. 11. The comparison between $\bar{a}_c$ (as a variation of $R_{\text{applied}}$) with (sold curve) and without (dash curve) residual stress effects, for a range of indentation depths $\delta/D$ with $\sigma_{\max}/\sigma_y = 1/2$. Cracks are located at the rim of deep indents.

small semi-circular-like crack ($a \ll w$) at the rim. In the limit $\delta/D = 0$, $c_r = 1.2$, for $\delta/D = 0.10$, $c_r = 1.38$, and for $\delta/D = 0.16$, $c_r = 1.64$.

The total stress intensity factor of the putative crack is $K = K_{\text{res}} + \Delta K$. As already remarked, the cyclic contribution, $\Delta K$, is influenced by the geometry of the FOD but not the residual stress. The residual stress affects $R \equiv K_{\min}/K_{\max} = (K_{\text{res}} + \Delta K_{\min})/(K_{\text{res}} + \Delta K_{\max})$. Combining the two contributions and introducing the normalizations above, one has

$$R(\bar{a}) = \frac{\sqrt{\bar{a}}(d_0 + d_1\bar{a}/\bar{w})/\sqrt{\bar{w}/\bar{D}} + c_r\sigma_{\min}\sqrt{4\bar{a}/\pi}/\sigma_Y}{\sqrt{\bar{a}}(d_0 + d_1\bar{a}/\bar{w})/\sqrt{\bar{w}/\bar{D}} + c_r\sigma_{\max}\sqrt{4\bar{a}/\pi}/\sigma_Y}. \tag{15}$$

The notation $R_{\text{applied}} = \Delta K_{\min}/\Delta K_{\max} = \sigma_{\min}/\sigma_{\max}$ introduced in Eq. (3) will be used to characterize the superimposed cyclic load. The role of the residual tensile stress is to increase $R$ above $R_{\text{applied}}$, thereby lowering the threshold cyclic stress intensity factor, $\Delta K_{\text{TH}}$, as can be seen from the threshold data in Fig. 3b.

The influence of various levels of FOD on threshold crack size, $\bar{a}_c = a_c/(\Delta K_{\text{TH}}^0/\sigma_Y)^2$, is shown in Fig. 11 for applied cyclic histories with $\sigma_{\max}/\sigma_Y = 1/2$. For a given value of $R_{\text{applied}}$, the critical value, $\bar{a}_c$, is computed as the value of $\bar{a}$ such that the threshold condition given by Eq. (4) is satisfied: i.e. $\Delta K/\Delta K_{\text{TH}}^0 \equiv \Delta K_{\text{TH}}/\Delta K_{\text{TH}}^0 = 1 + b_0 R + b_1 R^2 + b_2 R^3$. The FOD levels in Fig. 11 range from $\delta/D = 0$ (no FOD) to deep indents with $\delta/D = 0.162$. To reveal the relative importance of residual stress and geometry change, dashed curves are included in Fig. 11 that incorporate geometry change (through $c_r$) but neglect the contribution of residual stress by replacing Eq. (15) with $R = \sigma_{\min}/\sigma_{\max} = R_{\text{applied}}$.

FOD reduces the critical threshold crack size: the deeper the indent the greater the reduction. Indents having $\delta/D=0.1$ (corresponding to 200 m/s impacts for the Ti–6Al–4V substrates, cf. Fig. 7) produce significant reductions in critical crack size especially at low values of $R_{applied}$. Deep indents ($\delta/D = 0.16$, corresponding to 300 m/s impacts for the Ti–6Al–4V system) reduce the critical crack size by more than a factor of two over the entire range of $R_{applied}$. The roles of residual stress and geometry change associated with the FOD are brought out clearly in Fig. 11. At values of $R_{applied}$ above about 0.4, the dominant effect of FOD is due to the elastic stress concentration produced by the geometry of the impact crater. The effect of residual stress in this range is very small. At values of $R_{applied}$ below 0.4, residual stress becomes increasingly important. At $R_{applied} = 0.1$, residual stress is the more important of the two contributions to the reduction in the critical crack size. The importance of the residual stress at low values of $R_{applied}$ is readily understood in terms of the relatively large boost of $R$ due to the residual stress.

In FOD applications confronted in the aerospace industry, $R_{applied}$ is usually large due to the high mean stress associated with vibratory motion superimposed on the relatively high steady inertial stresses supported by the blades (Cowles, 1996; Mall et al., 2001). Therefore, one concludes that for most of the FOD problems in practice where indents are deep and $R_{applied}$ is large, the geometry effect is the most important factor in reducing fatigue life. The exception is in cases where $R_{applied}$ is low, for instance, in the parallel experimental studies by Peters et al. (2000, 2002) and Boyce et al. (2001b, 2002), where one must take into account the effect of residual stresses.

## 4.2. Cracking at low applied load ratio

At low $R_{applied}$, the residual stress field plays an important role in reducing $a_c$. There are a number of related issues that may be important, including the effect of finite specimen size and support on the residual stresses, non-normal impact and changes in residual stress due to subsequent stressing. Residual stresses turn out to depend rather strongly on the size of the specimen and the manner in which it is supported. For example, the Berkeley group (Peters et al., 2000, 2002) conducted normal impact tests on beam-type specimens whose thicknesses were on the order of the particle diameter. The combination of finite thickness and bending deformations produced residual stress distributions that were quite different from those for the deep substrate. Simulations of the beam-type specimens (Chen, 2001; Peters et al., 2002) were able to capture the stresses measured in the experiments.

FOD frequently occur as inclined impacts with incident angles roughly $30°$ or $60°$. Moreover, the impact site is often near the leading edge of the blades. A few non-axisymmetric calculations have been carried out for inclined impact of deep substrates (Chen, 2001; Peters et al., 2002). Qualitatively, the findings are similar to those reported here for normal impact. Roughly speaking, the residual stress field on the entrance side of an inclined impact looks similar to that of a shallow normal impact, while the stress on the exit flank is more like that of a deep normal impact, due to prominent plastic pile-up. The magnitudes of residual stresses for inclined impacts are about the same as those reported here for normal impacts.

The residual stress field may change during subsequent cyclic loading, especially if the remote cyclic stress is amplified by a local stress concentration. The Ti–6Al–4V alloy has a strong Bauschinger effect, and its yield stress on reversed loading, $\sigma_Y^R$, is considerably smaller than $\sigma_Y$ (Boyce et al., 2002). When the local compressive residual stress superimposed on the tensile applied cyclic stress exceeds $\sigma_Y^R$, the residual compressive stress at the bottom of the impact crater will be relaxed by 30–40%. These effects have been simulated and measured experimentally (Chen, 2001; Boyce et al., 2002).

Finally, we mention that the residual tensile stress at the sub-surface location (C in Fig. 9) has been observed to be a site for fatigue crack nucleation at low applied stress level ($\sigma_{max} = \frac{1}{3}\sigma_Y$), where the combination of cyclic and residual stress is not enough to cause stress relaxation (Peters et al., 2002). There is no elastic stress concentration at this subsurface location and the residual tensile $\sigma_{\theta\theta}$ is the only contribution expected to reduce the critical threshold crack size. The reduction of critical crack size associated with fatigue crack growth threshold can be estimated using the same approach proposed in previous sections. For example, one finds that for a 300 m/s FOD, $\bar{a}_c = 2.08$ when $\sigma_{max}/\sigma_y = 1/3$ and $R_{applied} = 0.1$. This compares with $\bar{a}_c^0 = 3.87$ where there is no FOD. The reduction of the critical crack radius is about 45% for subsurface fatigue cracking.

## 5. Concluding remarks

To provide basic insight into the mechanics of foreign object damage of turbine blades, this paper has addressed the residual stresses and geometric shape of indents caused by spherical particles impacting a deep elastic–plastic substrate at high normal velocity. The numerical results presented have been determined for materials with no strain hardening and moderate strain-rate sensitivity. The effect of the FOD on reducing the size of critical threshold fatigue cracks is also studied.

The main finding from the first part of the study on dynamic impact of a material with the rate sensitivity representative of blade material such as Ti–6Al–4V is that the normalized depth and width of the indent, $\delta/D$ and $w/D$, are primarily dependent on a single dimensionless kinetic energy parameter, $\Omega = KE/(\sigma_Y D^3) = \frac{\pi}{12}(\rho_p/\sigma_Y)v_0^2$. Typical values of this parameter for FOD fall in the range from 0.05 to 0.2 for turbine blade applications. Accounting for inertia of the substrate is important in determining the size of the indent, resulting in predicted depth reduction of about 20% compared to work-equivalent static indents. Material rate dependence further reduces the depth of the indent, roughly by an additional 20% for rate dependence typical of Ti–6Al–4V. On the other hand, for a given normalized depth of indent, $\delta/D$, the residual stress components important in altering fatigue life are essentially independent of inertial and material rate effects.

The effect of the residual stress and the indent geometry on the critical size of threshold fatigue cracks has been assessed for subsequently applied cyclic loading histories. For normal indents at $\Omega$-levels typical of those expected for FOD, both the residual stress and the geometric stress concentration factor are important when $R = \sigma_{min}/\sigma_{max}$ for the applied cyclic history is less than about 0.4. At higher values of $R$, common to

most high-cycle blade applications, only the geometric stress concentration is important. This finding, which has important implications for understanding and analyzing FOD, is likely to carry over to inclined impact and to impact at locations such as the leading edge of a blade.

In this paper, we have analyzed the effect of FOD on the critical size of a threshold fatigue crack. No attempt has been made to predict the effect of FOD on the number of cycles to fatigue crack initiation, or equivalently on the fatigue life. Experimental data on the threshold cyclic stress intensity such as that for Ti–6Al–4V in Fig. 3 is established on specimens with cracks which are generally much longer that the putative micro-cracks assumed in the present analysis. One cannot be certain that the data is applicable for cracks on the order of 50 μm, representative of the threshold crack predicted for the Ti–6Al–4V. Thus, the present results may only provide a qualitative assessment of FOD on the lifetime of the blades.

## Acknowledgements

## References

Boyce, B.L., Ritchie, R.O., 2001a. Effect of load ratio and maximum stress intensity on the fatigue threshold in Ti–6Al–4V. Eng. Fract. Mech. 68, 129–147.

Boyce, B.L., Chen, X., Hutchinson, J.W., Ritchie, R.O., 2001b. The residual stress state due to a spherical hard-body impact. Mech. Mater. 33, 441–454.

Boyce, B.L., Chen, X., Peters, J.O., Hutchinson, J.W., Ritchie, R.O., 2002. Mechanical relaxation of localized residual stress associated with foreign object damage. Int. J. Fatigue, submitted for publication.

Chen, X., 2001. Foreign object damage and fatigue cracking. Ph.D. Thesis, Harvard University.

Chen, X., Hutchinson, J.W., 2001. Foreign object damage and fatigue crack threshold: cracking outside shallow indents. Int. J. Fract. 107, 31–51.

Chen, X., Wang, R., Yao, N., Evans, A.G., Hutchinson, J.W., Bruce, R.W., 2002. Foreign object damage in a thermal barrier system: mechanisms and simulations. Mater. Sci. Eng. A, in review.

Clifton, R.J., 1983. Dynamic plasticity. J. Appl. Mech. 50, 941–952.

Cowles, B.A., 1996. High cycle fatigue in gas turbines—an industry perspective. Int. J. Fract. 80, 147–163.

Follansbee, P.S., Gray, G.T., 1989. An analysis of the low temperature, low and high strain-rate deformation of Ti–6Al–4V. Metall. Mater. Trans. 20A, 863–874.

Hibbit, Karlsson & Sorensen Inc., 1999. ABAQUS version 5.8 user's manual. Hibbit, Karlsson & Sorensen Inc., Pawtucket, RI.

Huang, Y., Hutchinson, J.W., Tvergaard, V., 1991. Cavitation instabilities in elastic–plastic solids. J. Mech. Phys. Solids 39, 223–241.

Larsen, J.M., Worth, B.D., Annis, C.G., Haake, F.K., 1996. An assessment of the role of near-threshold crack growth in high-cycle-fatigue life prediction of aerospace titanium alloys under turbine engine spectra. Int. J. Fract. 80, 237–255.

Mall, S., Hamrick, J.L., Nicholas, T., 2001. High cycle fatigue behavior of Ti–6Al–4V with simulated foreign object damage. Mech. Mater. 33, 679–692.

Mesarovic, S.D., Fleck, N.A., 1999. Spherical indentation of elastic–plastic solids. Proc. Roy. Soc. London Ser. A 455, 2707–2728.

Meyer, L.W., 1984. Titanium, science and technology. In: G. Lütjering, U. Zwicker, W. Bunk (Eds.), Deutsche Gesellschaft für Metallkunde, pp. 1851–1858.

Nicholas, T., 1999. Critical issues in high cycle fatigue. Int. J. Fatigue 21, 199–209.

Nicholas, T., Barber, J.P., Bertke, R.S., 1980. Impact damage on titanium leading edges from small hard objects. Exp. Mech. 20, 357–364.

Nicholls, J.R., Jaslier, Y., Rickerby, D.S., 1997. Erosion and foreign object damage of thermal barrier coatings. High Temp. Corrosion Prot. Mater. 4, 935–948.

Nisida, M., Kim, P., 1962. Stress concentration caused by the presence of a spherical cavity or a spherical-surfaced hollow. Proceedings of the 12th National Congress Applied Mechanics, pp. 69–74.

Peters, J.O., Roder, O., Boyce, B.L., Thompson, A.W., Ritchie, R.O., 2000. Role of foreign-object damage on thresholds for high-cycle fatigue in Ti–6Al–4V. Metall. Mater. Trans. A31, 1571–1583.

Peters, J.O., Boyce, B.L., Chen, X., McNaney, J.M., Hutchinson, J.W., Ritchie, R.O., 2002. On the application of the Kitagawa–Takahashi diagram to foreign object damage and high cycle fatigue. Eng. Fract. Mech. in press.

Ritchie, R.O., Davidson, D.L., Boyce, B.L., Campbell, J.P., Roder, O., 1999a. High-cycle fatigue of Ti–6Al–4V. Fatigue Fract. Eng. Mater. Struct. 22, 621–631.

Ritchie, R.O., Boyce, B.L., Campbell, J.P., Roder, O., Thompson, A.W., Milligan, W.W., 1999b. Thresholds for high-cycle fatigue in a turbine engine Ti–6Al–4V alloy. Int. J. Fatigue 21, 653–662.